J. Fluid Mech. (1972), *vol.* 54, *part* 4, *pp.* 577–598
Printed in Great Britain

On the breaking of standing internal gravity waves

By ISIDORO ORLANSKI
Geophysical Fluid Dynamics Laboratory/NOAA, Princeton University

(Received 17 December 1971 and in revised form 11 May 1972)

A solution has been found for the transient behaviour of resonant growing standing waves by using a perturbation expansion. Comparison with laboratory experiments as well as a numerical nonlinear solution of the same problem leads to the conclusion that: (i) the transient behaviour and the nonlinear tendency of the standing waves are described well by the analytic expression; (ii) the numerical results describe the solution very well until the wave starts to break; (iii) from the laboratory experiments and the numerical results, the standing internal gravity waves break owing to local gravitational instability at a critical amplitude which is similar to the one predicted by the expansion theory; (iv) the critical amplitude seems to be the maximum amplitude that a wave can reach; (v) when the generation of turbulence is violent, the small eddies begin forcing a secondary flow characterized by layers of strong jets separated by patches of turbulence.

1. Introduction

The importance of the breaking of internal gravity waves as a mechanism for generating turbulence in a stable stratified medium in the atmosphere and in the ocean was pointed out by Phillips (1966, ch. 5). He suggested that a Kelvin–Helmholtz instability is produced by the local shear of a slowly time-varying, finite amplitude internal gravity wave. On the other hand, Orlanski & Bryan (1969) have proposed another possible mechanism for generating turbulence and mixing. They suggested that a nonlinear effect such as the horizontal advection of density causes locally unstable density gradients. This effect, produced by the wave motion, is a common characteristic of growing waves.

To avoid the difficulty of making a controlled laboratory experiment with propagating waves, the author decided to examine a similar process, namely, the breaking of standing internal gravity waves. Waves forced to grow by a resonant process can develop large amplitudes, so the possibility of obtaining both types of instability existed since the waves had very low frequency and small growth rate. Some evidence of the mechanism of breaking standing waves has been previously mentioned by Thorpe (1968). However, he looked at interface waves and the cause of the breaking in his experiment was not quite clear.

The next three sections of this paper describe the governing equations, the initial-value problem and the second-order interactions. Section 5 will describe the experiment and the results, while §§ 6 and 7 are devoted to a discussion

of the breaking of standing waves and the damping effect on free standing waves, respectively.

2. Description of the model

Let us consider a two-dimensional container of length L and height H filled with a linearly stratified fluid of density $\bar{\rho} = \rho_0(1+\beta z)$. The motion of the fluid is forced by means of an oscillatory paddle at the top of the receptacle. The equations describing the flow are

$$\frac{\partial \mathbf{v}}{\partial t} + \mathbf{v}.\nabla\mathbf{v} = -\frac{1}{\rho_0}\nabla p - \mathbf{k}g\rho' + \nu\nabla^2\mathbf{v}, \tag{2.1}$$

$$\partial\rho'/\partial t + \mathbf{v}.\nabla\rho' + \beta w = \kappa\nabla^2\rho', \tag{2.2}$$

$$\nabla.\mathbf{v} = 0, \tag{2.3}$$

where $\mathbf{v}$ is the velocity vector with components u and w in the x and z directions respectively; ρ' is the density departure from $\bar{\rho}$ divided by ρ_0: $\rho' = (\rho - \bar{\rho})/\rho_0$. κ and ν are the molecular conductivity and molecular viscosity respectively, and $\mathbf{k}$ is the unit vector in the vertical direction.

The two-dimensionality of the motion allows some simplification of equations (2.1)–(2.3). The vorticity equation can be obtained by taking the curl of (2.1) and, using the conditions of (2.3), the velocity as well as the vorticity may be described by means of a stream function ψ; equations (2.1)–(2.3) are then reduced to the following:

$$\xi_t - J(\psi, \xi) = g\rho'_x + \nu\nabla^2\xi, \tag{2.4}$$

$$\xi = \nabla^2\psi, \tag{2.5}$$

$$\rho'_t - J(\psi, \rho') = \beta\psi_x + \kappa\nabla^2\rho', \tag{2.6}$$

where $u = \psi_z$ and $w = -\psi_x$.

Boundary conditions

For simplicity, free slip boundary conditions are used. At the side walls $x = 0, L$, $\psi = 0$ and $\xi = 0$, and at $z = \psi = 0$, $\xi = 0$. In order to simulate the oscillatory paddle at $z = H$ a condition is specified for the stream function, say

$$\psi(z = H) = F_0 \sin kx \sin \omega_0 t.$$

The adiabatic condition ($\partial\rho/\partial n = 0$ at the walls) was used for the density. To complete the set of equations, we fixed the initial conditions:

$$\psi = \rho' = 0 \quad \text{at} \quad t = 0. \tag{2.7}$$

Two important parameters in (2.1)–(2.6) are $N = (-g\beta)^{\frac{1}{2}}$, the Brunt–Väisälä frequency, and H, the depth of the container. Using these two parameters we non-dimensionalize the variables in the following way:

$$\chi = x/H, \quad \zeta = z/H, \quad t = TN, \quad l = L/H,$$
$$\phi = \psi/NH^2, \quad \Theta = (g/N^2H)\rho', \quad f_0 = F_0/NH^2, \quad \omega = \omega_0/N.$$

Then, rewriting (2.4)–(2.6) together with the boundary and initial conditions, we have

$$\nabla^2\phi_t - J(\phi, \nabla^2\phi) = \Theta_x + (1/Re)\,\nabla^2\nabla^2\phi, \tag{2.8}$$

$$\Theta_t - J(\phi, \Theta) = -\phi_x + (1/Re\,Pr)\,\nabla^2\Theta, \tag{2.9}$$

where $Re = NH^2/\nu$ is the Reynolds number and $Pr = \nu/\kappa$ is the Prandtl number,

$$\left.\begin{aligned} \phi = \Theta_x = 0 \quad &\text{at} \quad \chi = 0, l, \\ \phi = \Theta_\zeta = 0 \quad &\text{at} \quad \zeta = 0, \\ \phi = f_0 \sin(m\pi/l)\,\chi \sin\omega t \quad &\text{at} \quad z = 1, \end{aligned}\right\} \tag{2.10}$$

and the initial condition

$$\phi = \Theta = 0 \quad \text{at} \quad t = 0. \tag{2.11}$$

The full nonlinear system (2.8)–(2.11) was solved by numerical integration and will be discussed in a later section. In the next section we shall solve the first two orders of the solution by perturbation techniques.

3. Initial-value problem

In order to solve the system (1.8)–(1.11) by expanding the solution in powers of a small parameter $f_0 \ll 1$, say, we shall assume that the fluid is inviscid, i.e. $Re \to \infty$. As will be shown later, this is not a strong assumption since the characteristic values of Re and Pr in the experiments are 2×10^5 and 5×10^2 respectively.

Writing the stream function and density in powers of f_0 yields

$$\phi = f_0\phi_1 + f_0^2\phi_2 + O(f_0^3), \tag{3.1}$$

$$\Theta = f_0\Theta_1 + f_0^2\Theta_2 + O(f_0^3). \tag{3.2}$$

The inviscid forms of (2.8) and (2.9) to first order are

$$\nabla^2\phi_{1t} = \Theta_{1\chi}, \tag{3.3}$$

$$\Theta_{1t} = -\phi_{1\chi}, \tag{3.4}$$

with boundary conditions

$$\phi_1 = 0 \quad \text{at} \quad \chi = 0, l, \tag{3.5a}$$

$$\phi_1 = 0 \quad \text{at} \quad \zeta = 0, \tag{3.5b}$$

$$\phi_1 = \sin(m\pi/l)\,\chi \sin\omega t \quad \text{at} \quad \zeta = 1, \tag{3.5c}$$

and initial conditions

$$\phi_1 = \Theta_1 = 0 \quad \text{at} \quad t = 0. \tag{3.6}$$

The term Θ_1 is eliminated from (3.3) and (3.4) by differentiating (3.3) with respect to t and (3.4) with respect to χ, yielding

$$\nabla^2\phi_{1tt} = -\phi_{1\chi\chi}. \tag{3.7}$$

The Laplace transform of ϕ_1 is defined as

$$\hat{\phi}_1(s) = \int_0^\infty \phi_1 e^{st}\,dt. \tag{3.8}$$

Then, noticing that (3.3) and (3.6) imply that ϕ_1 and $\nabla^2\phi_{1t}$ are zero at $t = 0$, we may rewrite (3.7) as follows:

$$s^2\nabla^2\hat{\phi} = -\hat{\phi}_{\chi\chi}. \tag{3.9}$$

A solution of this equation that satisfies (3.5a) and (3.5b) is

$$\hat{\phi} = \hat{\phi}_{00}(s)\sin(p\pi/l)\,\chi\sinh\gamma\zeta, \tag{3.10}$$

where

$$\gamma = \frac{(p\pi/l)\,(1+s^2)^{\frac{1}{2}}}{s}.$$

At the boundary $\zeta = 1$,

$$\hat{\psi} = \sin\frac{m\pi}{l}\,\chi\left(\frac{\omega}{s^2+\omega^2}\right). \tag{3.11}$$

Note that the term $\omega/(s^2+\omega^2)$ is the Laplace transform of the forcing function.

Substitution of (3.10) into (3.11) determines the horizontal wavenumber $p = m$ and the amplitude, which is

$$\hat{\phi}_{00}(s) = \omega/(s^2+\omega^2)\sinh\gamma(s). \tag{3.12}$$

The inverse Laplace transform of (3.10) will give the time-dependent solution of the stream function:

$$\phi(\chi,\zeta,t) = \frac{\sin(m\pi/l)\,\chi}{2\pi i}\int_{\epsilon-i\infty}^{\epsilon+i\infty}\frac{\omega}{s^2+\omega^2}\,\frac{\sinh\gamma\zeta\,e^{st}}{\sinh\gamma}\,ds. \tag{3.13}$$

We shall not give the details for evaluating the integral here since the procedure is standard for this kind of problem; we shall only mention that the character of the poles of the integral (single or double) will describe the type of solution for ϕ (non-resonant or resonant). The roots s_i of $\sinh\gamma(s_i) = 0$ give the contribution to the internal gravity waves and the roots of $s^2+\omega^2 = 0$ give the forcing solution. Now, if any of the s_i is equal to $\pm i\omega$, the integrand of (3.13) has only single poles and the solution will be a superposition of the normal modes into which the forcing function was decomposed. In such case the non-resonant solution is

$$\phi_1 = \sin\frac{m\pi}{l}\,\chi\sin\omega t\,\frac{\sin\gamma\zeta}{\sin\gamma} + \sum_{q=1}^{\infty} a_q\sin q\pi\zeta\sin\omega_q t\sin\frac{m\pi}{l}\,\chi, \tag{3.14}$$

where

$$\gamma = (m\pi/l)\,(1-\omega)^{\frac{1}{2}}/\omega,$$

the frequency ω_q is given by

$$\omega_q = \frac{\pi m/l}{[(m\pi/l)^2+(q\pi)^2]^{\frac{1}{2}}}$$

and the Fourier coefficients for the free mode by

$$a_q = -2\frac{\omega_q}{\omega}\,\frac{q\pi(-1)^q}{\gamma^2-(q\pi)^2}.$$

The first part of the right-hand side of (3.14) is the forcing term and the second part represents the free modes that help the solution to satisfy the initial condition

$$\nabla^2\phi_{1t} = 0 \quad \text{at} \quad t = 0.$$

The density field, from (3.4), is

$$\Theta_1 = \frac{(m\pi/l)}{\omega}\frac{\sin\gamma\zeta}{\sin\gamma}\cos\frac{m\pi}{l}\chi\cos\omega t + \frac{m\pi}{l}\cos\frac{m\pi}{l}\chi\sum_{q=1}^{\infty}\frac{a_q}{\omega_q}\sin q\pi\zeta\cos\omega_q t \quad (3.15)$$

with the a_q defined as before. Θ_1 satisfies the initial condition $\Theta_1 = 0$ at $t = 0$.

Resonant wave

Resonance occurs when one of the s_i is equal to the forcing frequency $\pm i\omega$; then the integral has a double pole and the solution is of the form

$$\phi_1 = (-1)^n\left\{\zeta\cos n\pi\zeta\sin\omega t - \frac{m\pi}{(n\pi)^2+(m\pi/l)^2}\omega t\sin n\pi\zeta\cos\omega t\right\}\sin\frac{m\pi}{l}\chi + \sum_{q=1}^{\infty} b_q\sin q\pi\zeta\sin\omega_q t\sin\frac{m\pi}{l}\chi, \quad (3.16)$$

where $n = (m\pi/l)(1-\omega^2)^{\frac{1}{2}}/\omega$ is an integer and

$$b_q = \begin{cases} \dfrac{-2q\pi\omega_q(-1)^{q+n}}{[(q\pi)^2-(n\pi)^2]\omega} & \text{for} \quad q \neq n, \\ \dfrac{1}{2n\pi} - \dfrac{n\pi}{(n\pi)^2+(m\pi/l)^2} & \text{for} \quad q = n. \end{cases}$$

The first-order density perturbation field is given by

$$\Theta_1 = (-1)^n\frac{m\pi}{l}\cos\frac{m\pi}{l}\chi\left\{\frac{\zeta}{\omega}\cos n\pi\zeta\cos\omega t + \frac{n\pi}{(n\pi)^2+(m\pi/l)^2}\sin n\pi\zeta\left(t\sin\omega t + \frac{1}{\omega}\cos\omega t\right)\right\} + \frac{m\pi}{l}\sum_{q=1}^{\infty}\frac{b_q}{\omega_q}\cos\omega_q t\sin q\pi\zeta\cos\frac{m\pi}{l}\chi. \quad (3.17)$$

Note that the terms in the stream function (3.16) completely satisfy the initial condition. The free modes are excited only to adjust the density field to zero at the initial time. We may also notice that there is a leading term which is proportional to t and out of phase with the forcing function; this term will grow linearly in time until nonlinear effects become important. Only this part of the solution will be considered in the calculation of the second-order effect.

4. Second-order interaction

By expanding (2.8)–(2.9) to the second order we obtain

$$\nabla^2\phi_{2t} - \Theta_{2\chi} = +J(\phi_1, \nabla^2\phi_1), \quad (4.1)$$

$$\Theta_{2t} + \Theta_{2\chi} = J(\phi_1, \Theta_1), \quad (4.2)$$

and the boundary conditions (2.10) to second order are

$$\left.\begin{aligned} \phi_2 &= 0 \quad \text{at} \quad \chi = 0, l, \\ \phi_2 &= 0 \quad \text{at} \quad \zeta = 0, 1. \end{aligned}\right\} \quad (4.3)$$

Since the boundary conditions of (2.10) are sinusoidal in x and completely satisfy the first-order solution, the excitation of the second-order terms will be through the interior flow, owing to the interaction of the first-order terms, and not a result of conditions at the boundary. (This is not quite true in the experiment however. Since our paddle is not sinusoidal, the Fourier coefficients of the paddle forcing function are proportional to $(1/m\pi)^2$ for $m = 2, 6, 10, \ldots$ and zero for any other value. The paddle amplitude is then $z_0 \cos 2\pi x + \frac{1}{9} z_0 \cos 6\pi x + \ldots$. It seems quite justifiable to assume that the first term of the Fourier expansion is the most important since the amplitudes of the higher components are very small and also because the paddle's oscillation corresponds to resonant frequencies for wavenumber 1, which means that the other wavenumbers will not be sufficiently excited.)

The initial conditions, as before, are

$$\phi_2 = \Theta_2 = 0 \quad \text{at} \quad t = 0. \tag{4.4}$$

The Jacobians $J(\phi_1, \nabla^2\phi_1)$ and $J(\phi_1, \Theta_1)$ can be computed directly from (3.15) and (3.16). Without loosing generality we may simplify the expression for each Jacobian by using only the leading terms from the stream function and density, which is mainly the interaction of the linear growing solution from (3.15) and (3.16), since these will be the predominant parts after a few periods of oscillation.

In such a case, the first-order vorticity is a function of the stream function and, therefore, $J(\phi_1, \nabla^2\phi_1)$ is zero. However, it is not so for the density, the Jacobian being given by

$$J(\phi_1, \Theta_1) = \frac{(n\pi)^3 (m\pi/l)^2 \omega^2 t^2}{4\omega[(n\pi)^2 + (m\pi/l)^2]^2} \sin 2\omega t \sin 2n\pi\zeta. \tag{4.5}$$

Since this Jacobian is not a function of χ, a simple solution can be found through a time integration of (4.2) for the second-order correction:

$$\Theta_2 = \frac{(n\pi)^3}{8[(n\pi)^2 + (m\pi/l)^2]} [(-\omega^2 t^2 \cos 2\omega t + \omega t \sin 2\omega t + \tfrac{1}{2}\cos 2\omega t) \sin 2n\pi\zeta - \tfrac{1}{2} \sin 2n\pi\zeta]. \tag{4.6}$$

The expression in square brackets results from integrating the Jacobian (4.5). Notice, however, that this term does not satisfy the initial conditions. In order to do so, a function of ζ (the last term in the brackets) is subtracted. This term is also a solution of the second-order system.

So, the dimensional stream function and density perturbation to the second order for the resonant case are

$$\psi = F_0 \left\{ (-1)^n \left[\frac{z}{H} \cos \frac{n\pi}{H} z \sin \omega_0 t - \frac{n\pi\omega_0 t}{H^2[(n\pi/H)^2 + (m\pi/L)^2]} \sin \frac{n\pi z}{H} \cos \omega_0 t \right] + \sum_{q=1}^{\infty} \frac{b_q}{H} \sin \frac{q\pi}{H} z \sin \omega_q t \right\} \sin \frac{m\pi}{L} x \tag{4.7}$$

and

$$\rho' = \frac{\bar{\rho}_z}{\rho_0}\Bigg\{-\left(\frac{m\pi}{L}\right)F_0\Bigg[(-1)^n\left(\frac{z}{H\omega_0}\cos\frac{n\pi}{H}z\cos\omega_0 t + \frac{1}{H}\frac{n\pi/H}{[(n\pi/H)^2+(m\pi/L)^2]\,\omega_0}(\omega_0 t\sin\omega_0 t+\cos\omega_0 t)\sin\frac{n\pi}{H}z\right) + \sum_{q=1}^{\infty}\frac{b_q}{H\omega_q}\cos\omega_q t\sin\frac{q\pi}{L}z\Bigg]\cos\frac{m\pi}{L}x - \frac{F_0^2}{8H^2}\frac{(m\pi/L)^2\,(n\pi/H)^3}{\omega_0^2\,[(m\pi/L)^2+(n\pi/H)^2]^2} \times[(\omega_0 t)^2\cos 2\omega_0 t-\omega_0 t\sin 2\omega_0 t-(\tfrac{1}{2}\cos 2\omega_0 t-\tfrac{1}{2})]\sin 2\frac{n\pi}{H}z\Bigg\}. \qquad (4.8)$$

The experiment and the comparison between the experimental results and the expressions shown here will be described in the next section.

5. Description of the experiment

The apparatus used in the experiment (see figure 1, plate 1) consists of a rectangular tank (*a*) (87·5 cm deep, 150 cm long and 30 cm wide) which is entirely made of Perspex. At the top of the tank are two paddles (*b*), each of which pivot at a distance equal to a quarter of the length of the tank. The join between the paddles, which is made of rubber, is connected through a scotch yoke to a motorized variable-speed transmitter (*c*). Consequently, the paddles will have a rhythmic oscillation such that the frequency can be controlled by the motor's speed and the amplitude can be controlled by the centre of the arm. A counter automatically recorded the number of paddle oscillations.

The fluid in each experiment was a solution of salt and water, linearly stratified with height. The profile was achieved by filling the tank very slowly with a brine solution which came from mixing the fluids of both containers (marked (*d*) in figure 1). The container on the left is filled with a brine solution which is at the density desired at the bottom of the tank (*a*); the one on the right was filled with water. A description of the method will not be given here since it is well documented in Fortuin (1960). A piece of tubing connects the receiver (*e*) with the system (*a*)-(*d*) in such a manner that a dye can be added to the solution at any time to aid visualization of a specific layer.

Density measurements were made by two different methods: (i) using conductivity probes and (ii) using small pieces of glass. In the first method different types of probes were used, but they were mostly of the exposed electrode type, such as that shown at (*h*) in figure 1. The probe is a multi-electrode type with four channels to measure the time variation of density at four different levels. The probe was connected to a multichannel bridge system and a graph which recorded the signals. To measure the mean profile, a two-electrode probe was used. The probe was moved vertically in the fluid by a motorized device (*f*), thus giving direct measurements (about 60 over a 70 cm height) of the mean profile. The conductivity reading was made with a conductivity probe (YSI model 31, accuracy $\pm 1\,\%$) and an a.c. bridge (*g*).

In the other method, eight different coloured pieces of glass were used for

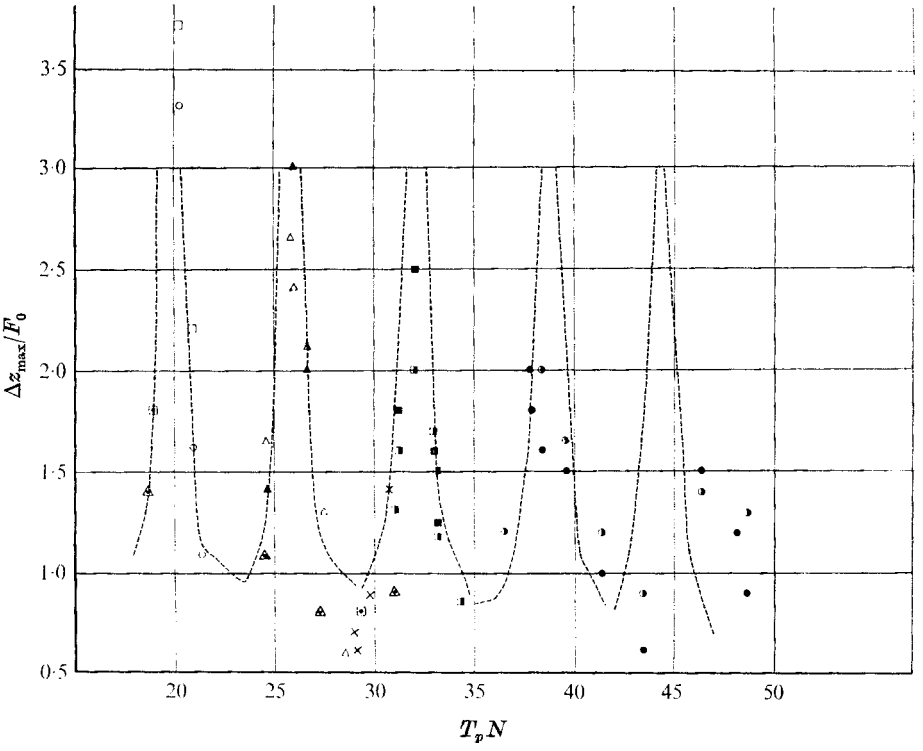

FIGURE 2. The maximum disturbance amplitude normalized by the forcing amplitude versus the normalized paddle period.

a quick check and as a control calibration for the conductive probes. The pieces were 0·3 cm in diameter and the precision was about $\Delta\rho/\rho = 10^{-3}$.

Measurement of forced response vs. frequency

In order to find the standing resonant waves we proceeded in the following manner. First, the density profile was measured; second, the Brunt–Väisälä frequency, i.e. $N = (-g\bar{\rho}_z/\rho_0)^{\frac{1}{2}}$, was computed; third, the period of the chosen vertical wavenumber was estimated and fourth, the probes were fixed at the levels where the maximum density disturbances would occur.

After these steps had been completed, different cases were tested by varying the frequency of the paddle near the estimated resonance value. Some of the results are shown in figure 2, in which the maximum amplitude of the disturbance, normalized by the amplitude of the paddle, is plotted against the period of the paddle, normalized by the Brunt–Väisälä frequency. The dots fall in peaks corresponding to vertical wavenumbers $n = 3$, 4, 5, 6 and 7 respectively. The dashed curves are obtained from the analytic expression of (3.15) for the non-resonant case. The infinite series for the free mode was approximated by considering only the first 20 modes. The graph shows that the first three peaks are in good agreement with the data, i.e. those for $n = 3$, 4, and 5, whereas the lack of such consistency for $n = 6$ and 7 is most likely due to an error in the level of

	Experiment											
	I	II	III	IV	V	VI	VII	VIII	IX	X	XI	XII
N (s^{-1})	0·653	0·663	0·6487	0·6562	0·598	0·6031	0·602	0·725	0·730	0·692	0·688	0·720
Test no.												
1	52·5	73·44	44·0	36·5	48·5	49·0	47·0	28·5	41·0	40·4	40·0	47·0
2	50·75	80·0	42·5	34·2	51·2	49·0	51·5	32·2	41·0	42·2	43·0	49·0
3	50·5	70·0	41·0	32·5	49·9	31·5	51·6	33·0	41·0	41·9	41·9	46·0
4	49·0	68·0	39·9	32·0	49·5	—	51·0	33·2	41·1	43·1	43·6	45·5
5	49·0	72·5	40·0	31·0	51·0	—	31·0	33·1	41·0	43·2	43·9	—
6	48·0	65·5	37·8	—	49·8	—	41·0	32·8	41·0	43·3	45·0	—
7	51·0	62·5	—	—	51·0	—	41·0	33·0	60·2	44·1	45·0	—
8	47·5	62·5	—	—	51·5	—	—	33·8	—	44·0	—	—
9	—	58·5	—	—	—	—	—	34·0	—	43·5	—	—
10	—	57·5	—	—	—	—	—	33·0	—	44·2	—	—
11	—	55·0	—	—	—	—	—	—	—	43·1	—	—
12	—	—	—	—	—	—	—	—	—	43·3	—	—
13	—	—	—	—	—	—	—	—	—	43·4	—	—
14	—	—	—	—	—	—	—	—	—	41·9	—	—
15	—	—	—	—	—	—	—	—	—	44·1	—	—
16	—	—	—	—	—	—	—	—	—	43·9	—	—
17	—	—	—	—	—	—	—	—	—	44·0	—	—
18	—	—	—	—	—	—	—	—	—	43·8	—	—
19	—	—	—	—	—	—	—	—	—	43·9	—	—
20	—	—	—	—	—	—	—	—	—	43·0	—	—

TABLE 1. A summary of the experiments conducted and the paddle frequency of each. The dimensional period of each test is also shown

the probe, which is quite critical. Accordingly, since the wavelength of these latter modes is small, a small variation in the height of the probe can result in large errors in the wave amplitude.

Time-dependent behaviour of experimental and theoretical results

Table 1 shows the different experiments which were done and the paddle frequency for each one. In addition to this, the dimensional period is also shown.

A characteristic of resonant waves, e.g. (3.16), is that at the initial time the wave has a linear growth. The density amplitude, as a function of time, can be expressed as

$$|\rho'| = \frac{\bar{\rho}_z F_0 mn}{\rho_0 H^2 L[(n/H)^2 + (m/L)^2]} t. \tag{5.1}$$

Notice that this expression is the term which directly involves $\omega_0 t$ in (3.16). Also, the term which is proportional to z is not considered because the amplitudes in the lower part of the tank, where $z/H < 1$, cause the term proportional to z/H to be small compared with right-hand side of (5.1), which is proportional to t.

The wave displacement can be written from (5.1) as

$$\Delta z = \frac{4F_0}{LH^2} \frac{n}{n^2/H^2 + (2/L)^2} t, \tag{5.2}$$

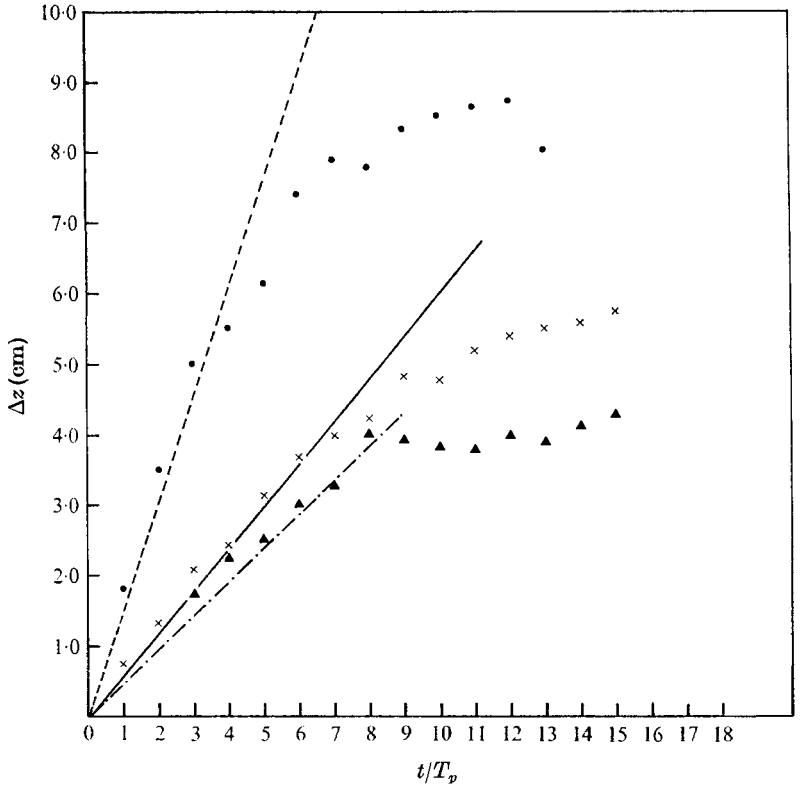

FIGURE 3. The displacement amplitude as a function of t/T_p at different vertical wavenumbers and paddle amplitudes. The points denote the experimental values and the straight lines represent the theoretical values. – – –, ●, $z_0 = 1{\cdot}2$ cm, $m = 3$; ——, ×, $z_0 = 0{\cdot}6$ cm, $m = 4$; —·—, ▲, $z_0 = 0{\cdot}6$ cm, $m = 5$. $\Delta z = 4[z_0 m/(m^2+1)]\, t/T_p$.

for $m = 2$, remembering that F_0 is the amplitude of the forcing stream function and also that its relation to the actual paddle displacement is

$$F_0 = (L/T_p)\, z_0 \tag{5.3}$$

where T_p represents the dimensional period. Then (5.2) can be rewritten as

$$\Delta z = 4 z_0 \frac{n}{n^2+1} \frac{t}{T_p} \quad \text{when} \quad L = 2H. \tag{5.4}$$

Figure 3 shows the predicted amplitude (5.4) (straight lines) and the observed amplitudes (dots) as a function of t/T_p for different vertical wavenumbers and different paddle amplitudes z_0. A linear growth behaviour is observed for about six or seven periods, after which the amplitudes level off. The wave has a large amplitude, and higher-order effects may account for this change.

Finite amplitude effects

Three different finite amplitude standing waves corresponding to vertical wavenumbers $n = 3$, 4 and 5 can be seen in figure 4 (plate 2). Experiments for $n = 6$ and 7 were conducted but their discussion will follow later. The scale in the middle

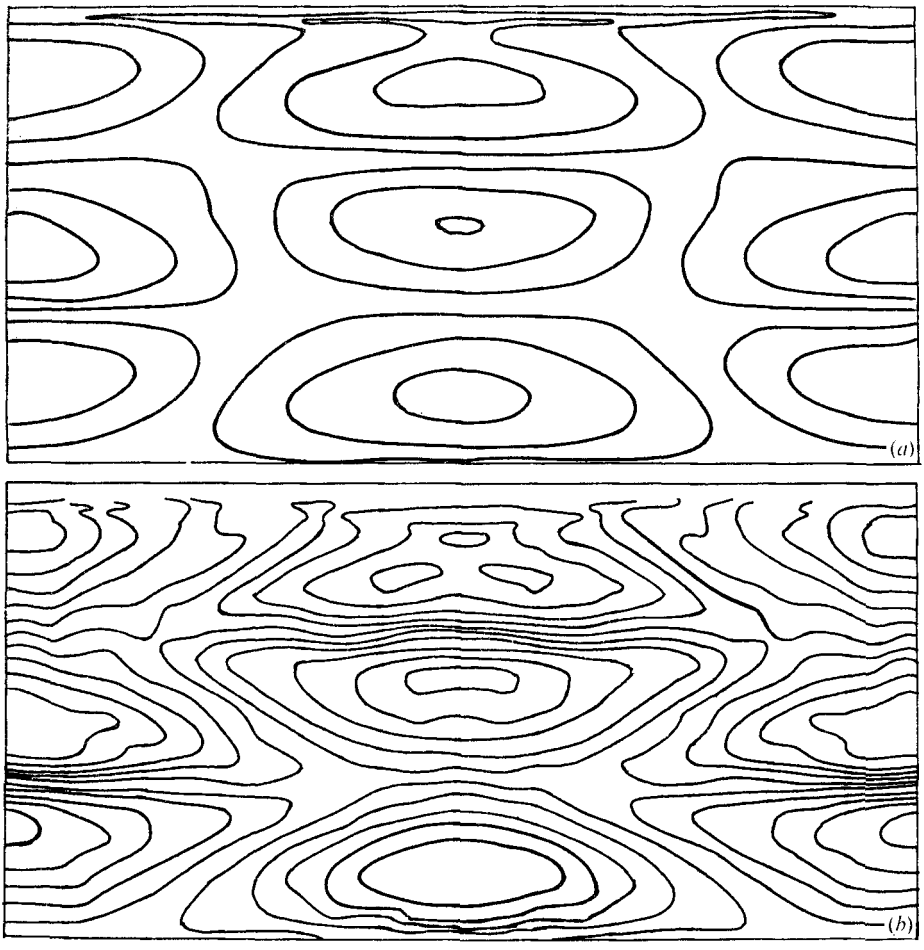

FIGURE 6. Two stages of the standing waves' growth for $n = 3$. (*a*) A regular pattern which is well described by the linear theory; $t = 6$ periods. (*b*) The effect of horizontal advection, indicated by the mushroom shape; $t = 12$ periods.

of the tank is marked at intervals of 2·54 cm and the actual visualization in the pictures is through eight dye layers, each initially 3·7 cm thick and equally separated by non-coloured layers, each 7 cm thick.

The standing waves grow for a few periods as the linear theory predicts; the shape of the density pattern is sinusoidal and the frequency is one close to resonance. However, since the amplitude of the forcing was deliberately chosen to be large, the nonlinear effect predicted by (4.8) is noticeable in the experiment after only a few periods of oscillation.

Figure 5(*a*) (plate 3) shows the wave shape after 20 periods corresponding to a vertical wavenumber of 3; the amplitude Δz is about 8·75 cm and the shape of the density pattern is no longer sinusoidal. Notice also that the trough and crest are becoming flat. A similar effect can be observed in a solution obtained by numerically integrating a set of finite difference equations corresponding to (2.8) and (2.9). Using the same boundary and initial conditions (2.10) and (2.11), the

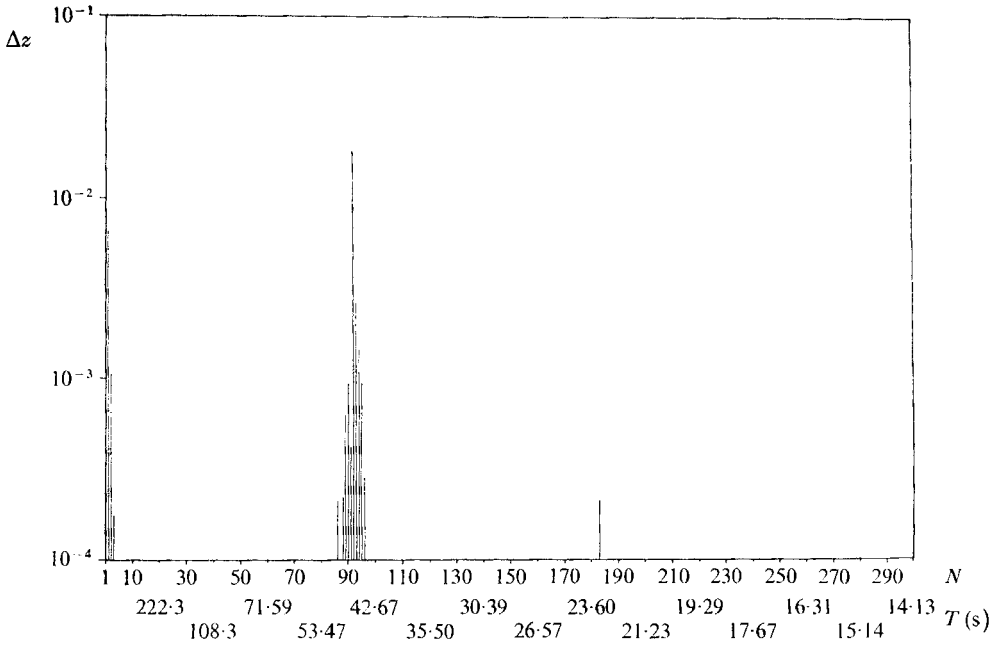

FIGURE 7. Fourier components for the conductivity response *vs.* the period; the main peak corresponds to the resonance period (46·42 s) and the secondary peak to the nonlinear interaction (23·21 s).

solutions described in the paper are for $Re \approx 10^5$ and $Pr = 500$. Although other results are not shown, different values were used for the parameters and in one case an eddy type of variable viscosity was included. These results will appear in a forthcoming paper on the numerical simulation of internal gravity waves. The numerical procedure and computer program used was developed by Lipps (1971) for studies on convection in the presence of shear flows. Grid points are located such that $Dx = \frac{1}{32}L$ and $Dz = \frac{1}{122}H$. This spacing gives a resolution of about thirty points in each direction over the dimensions of an internal wave resonant with the forcing. Observe that figure 5(*b*) (plate 3) shows the pattern of the numerical solution with the flatness effect.

The characteristic behaviour of the numerical solution can be described by the second-order term that affects the perturbed density field (4.8): the simple superposition of a single ellipsoidal cell given by the linear part Θ_1 and Θ_2, the second-order correction, which is a function of z and t only, thus modifying the density perturbation to a mushroom shape. In figure 6(*a*) we can see how the numerical solution for the perturbed density, after 6 periods, exhibits strong symmetry with a sinusoidal dependence in z ($\Theta_1 \propto \sin(3\pi/H)z$). After ten more periods, the horizontal advection of density becomes more important and, as expected, the mushroom shape results as shown in figure 6(*b*). Recall that this type of solution is the effect of the second-order terms ($\Theta_2 \propto \sin(6\pi/H)z$). This effect will try to flatten the isotherm. Finally, owing to horizontal advection, the heavier fluid will be carried over the lighter fluid, producing an unstable gradient of density that will produce overturning. This point will be elaborated

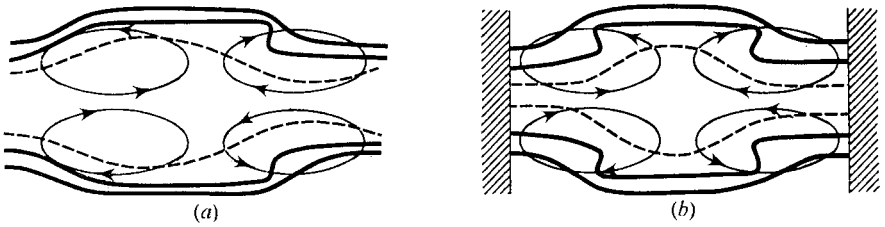

FIGURE 8. Sketch of the density and stream function for (*a*) propagating and (*b*) standing waves.

in the next section, where the breaking process is discussed. From the probe responses a Fourier analysis was made with respect to time, and the results show the presence of a peak at $2\omega_0$ for most of the laboratory experiments. An example is shown in figure 7, where the resonant period (experiment XII, 4, table 1) is 46·42 s and the peak appears at 23·21 s. This is in complete agreement with the second-order solution (4.6), in which the predominant term has a frequency of $2\omega_0$.

6. Breaking of standing waves

The principal objective of this paper is to identify the processes which cause internal gravity waves in confined regions to break into sporadic patches of turbulence. We hope that this simple case will allow us to gain some insight into the more complicated phenomena relevant to CAT (clear air turbulence) in the atmosphere and DOT (deep oceanic turbulence) in the ocean.

In laboratory experiments (Thorpe 1968; McEwan 1971) some types of breaking standing internal waves have also been observed. In this particular context, the expression 'breaking' does not imply total collapsing of the wave, but rather an abrupt transition from the smooth shape of the wave to a more disturbed one in which higher wavenumbers are generated.

A mechanism for the formation of the thermocline step structure (Orlanski & Bryan 1969), along with the related process of turbulence generation (DOT) in the ocean (Orlanski 1971), has been proposed in which these effects (which are less dependent on the local Richardson number and are affected more by the way in which the internal gravity waves become finite amplitude waves) are the result of sporadic overturning associated with finite amplitude internal gravity waves. Unstable gradients of density may develop locally in the wave; accordingly, a criterion for the required critical amplitude, that is, $\partial\rho/\partial z \geqslant 0$, was derived. Under this condition, the horizontal advection must balance the local time change of density; $\rho_t \simeq \mathbf{v}_H . \nabla\rho$. For a single wave, this condition is fulfilled if the horizontal velocity is larger than or equal to the horizontal component of the phase velocity of the wave ($|\mathbf{v}_H| \geqslant |\mathbf{c}_{ph}|$). In order to see the analogy between the breaking of propagating internal gravity waves and standing waves, let us consider figure 8.

The stream function and density field of a propagating wave are shown in figure 8(*a*). The ellipsoids represent the stream function at one instant; the dashed sinusoidal curves represent the isopycnics which result from a linear

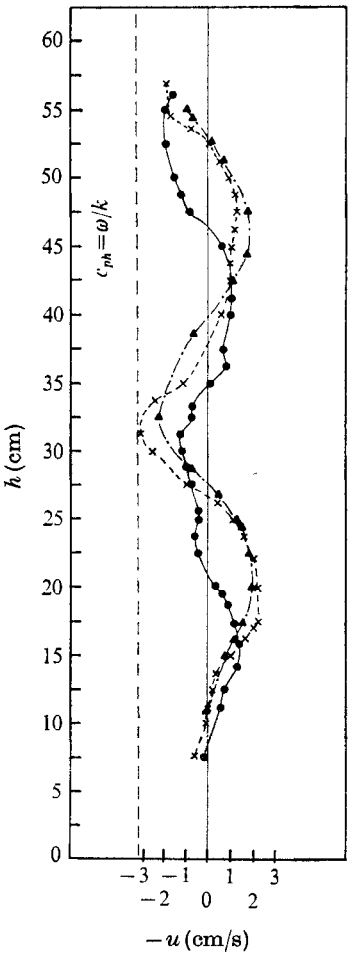

FIGURE 9. Horizontal velocity profile at $x = \frac{1}{4}L$ as a function of height. The wavenumber for all cases is 5. ▲, $t = 15$ periods; ×, $t = 19$ periods; ●, $t = 25$ periods.

theory, whereas the solid curves are the isopycnics which result from the nonlinear interaction. The strong horizontal advection in parts of the wave tries to push heavier fluid over lighter fluid, causing an S-shape in the isopycnics as shown. The entire process is possible because the stream function and density field are not exactly in phase. This condition is only possible for waves that are slowly growing, as is discussed in Orlanski & Bryan (1969). However, for pure neutral propagating waves the density field and stream function are exactly in phase and density advection is zero.

The stream function and density field are ninety degrees out of phase for standing waves as we can see in figure 8(*b*). The stream function changes sign every half period. We may notice, however, that a similar distortion will occur in this case owing to the strong horizontal advection of the wave. The main difference here is that the front and rear of the wave will be distorted. It should also be pointed out that the velocity of the particles must be larger than the change in the wave field in order to produce unstable density gradients. In such

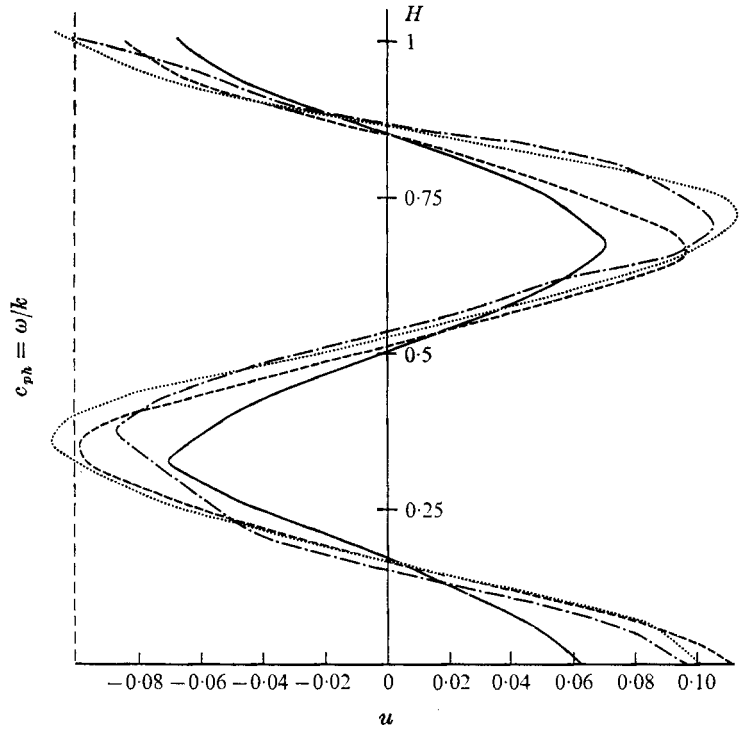

FIGURE 10. Horizontal velocity as a function of height from the numerical model for the vertical wavenumber $n = 3$. ——, $T = 168$; – – –, $T = 228$; ·····, $T = 278$; —·—, $T = 290$.

a case, the horizontal velocity u, as in the case of propagating waves, is given approximately by $\omega_0/(2\pi/L)$.

In the experiment, the tracers, which are very small pieces of plastic, were photographed over a certain time Δt (of the order of a tenth of the period), thus enabling the velocities to be calculated. The method is not particularly accurate when the time interval is a large fraction of the total period, nevertheless, it is a good means of obtaining a complete view of the flow. The amount of error in the velocities can be reduced if we account for the fact that there will be variations in the velocity along the trajectory.

Figure 9 shows the horizontal velocity profile at a fixed point ($x = \frac{1}{4}L$) as a function of height at three different times. For these cases the vertical wavenumber is 5 (experiment XII, 4). Note that the complete tank height (77 cm) is not shown in the graph because the pieces of plastic were not uniformly distributed throughout the tank. The triangles correspond to time $t = 15$ periods, before breaking, the crosses correspond to $t = 19$ periods, at breaking, and the circles to $t = 25$ periods, after breaking. The maximum velocity reached at the time of breaking was $u \simeq (\omega/2\pi)\, L = 3{\cdot}26$ cm/s.

Figure 10 is an analogous profile for the numerical solution when $n = 3$. Similar features can be identified in figures 9 and 10, which let us draw two important conclusions. First, breaking occurs at the predicted amplitude, which implies gravitationally unstable processes. Second, after breaking, the amplitude

of the velocity exhibits no further growth, implying that the critical amplitude is the maximum amplitude of the waves.

To estimate the amplitude for the density perturbation we shall use the vorticity equation (2.4). However, since the advection of vorticity is practically zero to higher orders (see equation (4.6)), the time change in vorticity will be given by

$$\xi_t = -[(m\pi/L)^2 + (n\pi/H)^2]\,\omega_0\psi = g\rho'_x \tag{6.1}$$

and the maximum amplitude of the stream function to that order is

$$|\psi|_{\max} \simeq |\mathbf{c}_{ph}|/\phi = \omega_0 LH/mn\pi^2, \tag{6.2}$$

where $\mathbf{c}_{ph}$ is ω/κ. It follows, then, that the maximum amplitude for the density perturbation is

$$|\rho'|_{\max} = \frac{[(m\pi/L)^2 + (n\pi/H)^2]}{n\pi^3 m^2}\frac{\omega_0^2}{g}L^2H. \tag{6.3}$$

This equation can be simplified if we remember that

$$\omega_0^2 = \frac{(-g\bar{\rho}_z/\rho_0)\,(m\pi/L)^2}{(m\pi/L)^2 + (n\pi/H)^2}.$$

Substituting this into (5.3) yields

$$|\rho'|_{\max} = \frac{\bar{\rho}_z}{\rho_0}\frac{1}{\phi}. \tag{6.4}$$

Note that a similar result can be obtained if the condition $\rho'_z = \bar{\rho}_z$ is used with the first-order solution of the density perturbation (3.16) and we neglect the higher orders. However, (6.4) is a more general result since no assumptions are made about the second-order density terms. Finally, the density expression (4.8) for the leading terms to a second-order approximation can be written as

$$\rho \simeq (\bar{\rho}_z/\rho_0)\,[z + \delta \sin\phi z \cos kx \sin\omega t + \tfrac{1}{8}\delta^2\phi \sin 2\phi z \cos 2\omega t + O(\delta^2/\omega t)], \tag{6.5}$$

where $\delta = [(-1)^n k\phi F_0/H\omega(k^2+\phi^2)]\,\omega t$, $k = 2\pi/L$ and $\phi = n\pi/H$.

From the conditions of (6.4), δ is about of the order of $1/\phi$. Then the second-order terms in the density equation are $\frac{1}{8}$ of the first-order ones, so the former can be neglected. It should be pointed out, however, that this condition will not be true when ρ'_z is computed since the second and higher orders have larger vertical wavenumbers and may be quite significant.

Now, rewriting (6.5) to first order, we have

$$\rho \simeq \frac{\bar{\rho}_z}{\rho_0}\left(z + \frac{1}{\phi}\sin\phi z \cos kx \sin\omega t\right). \tag{6.6}$$

From the expression (6.6) it can be shown that the maximum displacement between crest and trough of the isopycnic is given by

$$(\Delta z)_{\max} = \delta \cos[\Delta z_{\max}\phi]; \tag{6.7}$$

the value of the maximum displacement that satisfies the conditions of (6.7) is given by

$$(\Delta z/H)_{\max} \simeq 0{\cdot}739/\pi n. \tag{6.8}$$

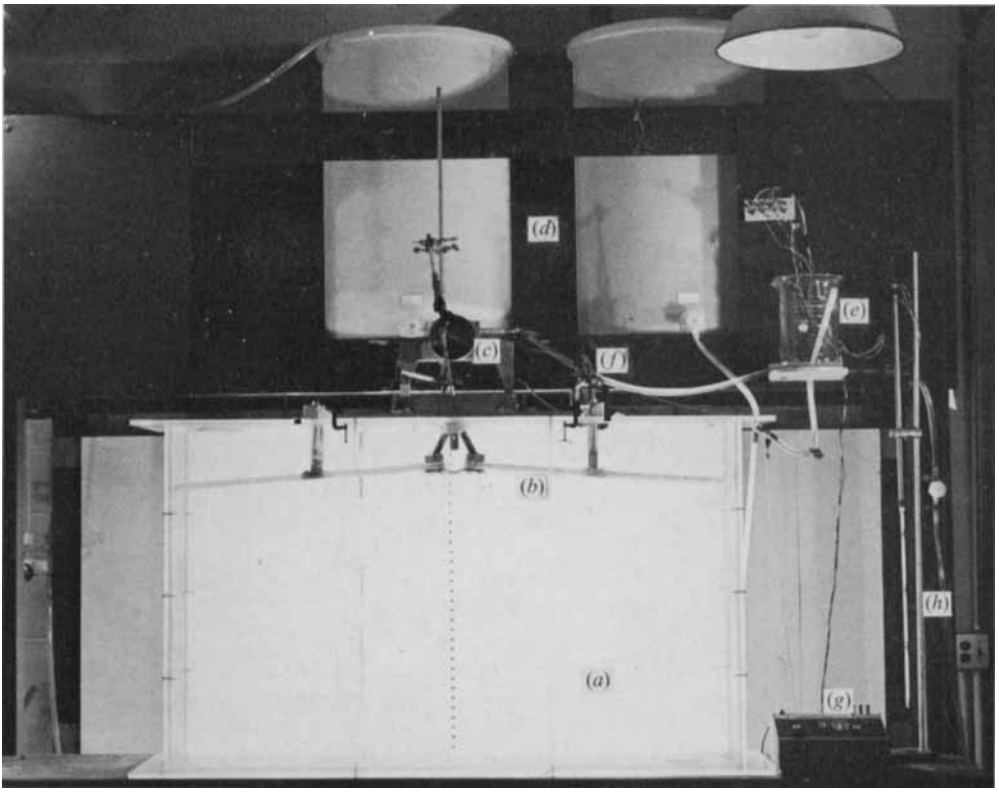

FIGURE 1. The experimental apparatus and measuring devices: (*a*) the tank, (*b*) the paddles, (*c*) the variable speed transmitter, (*d*) the fluid containers, (*e*) the receiver, (*f*) the motor, (*g*) an a.c. bridge, (*h*) the conductivity probe.

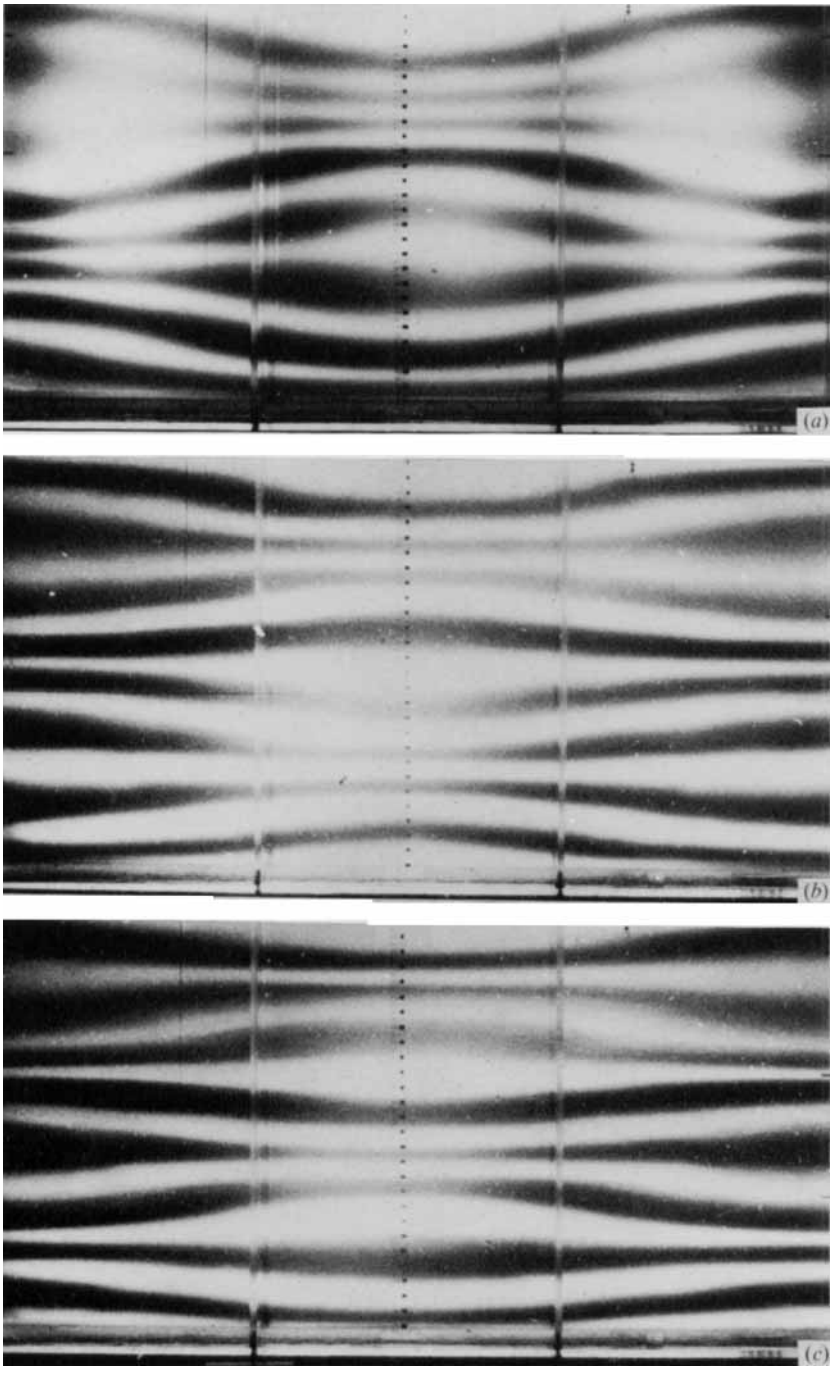

FIGURE 4. Pictures taken during the experiment showing finite amplitude standing waves. (*a*) Vertical wavenumbers $n = 3$. (*b*) $n = 4$. (*c*) $n = 5$.

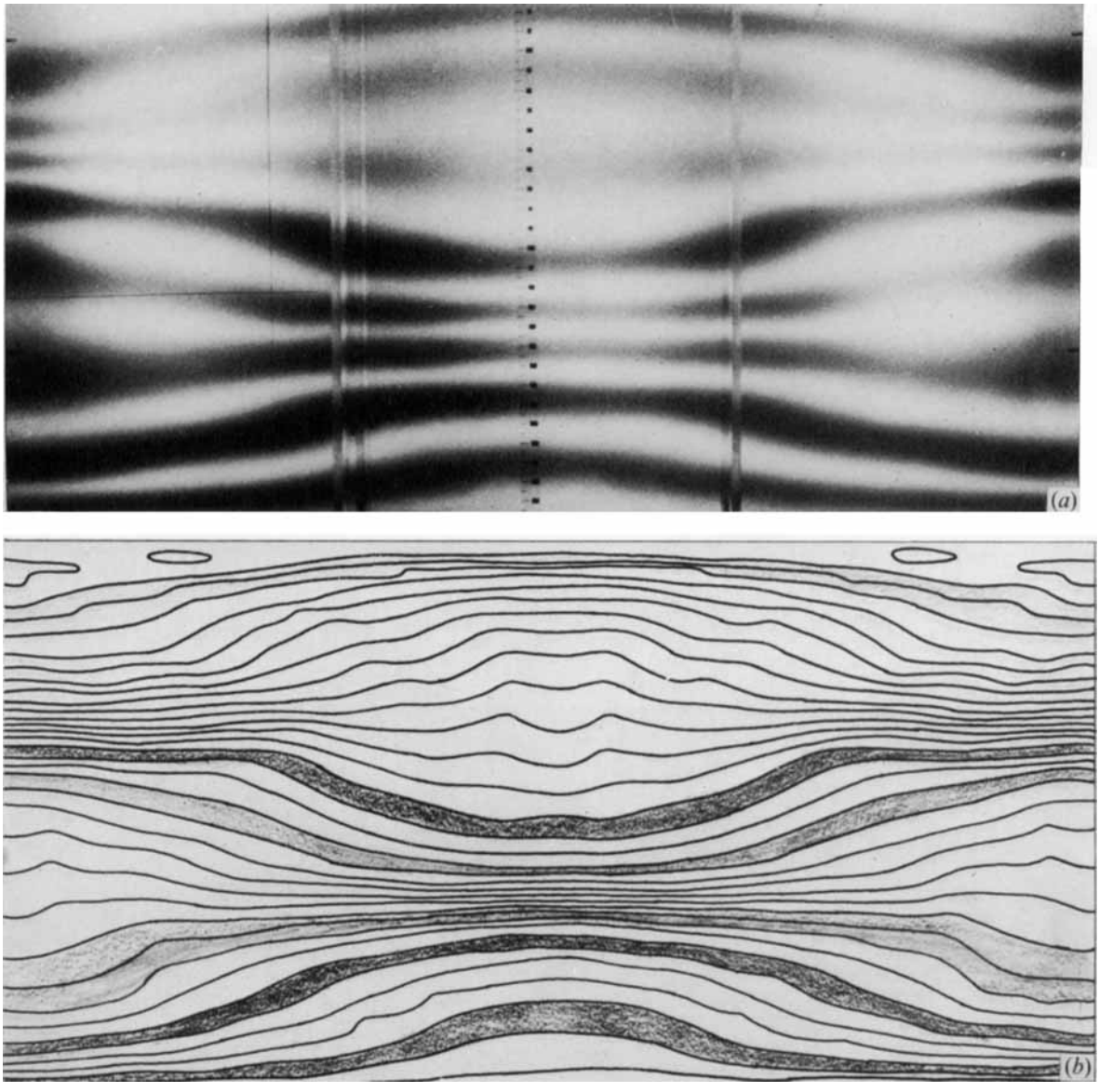

FIGURE 5. Comparison between (*a*) the actual experiment and (*b*) the numerical experiment at the same wavenumber, illustrating the flatness effect in the trough and crest of the waves.

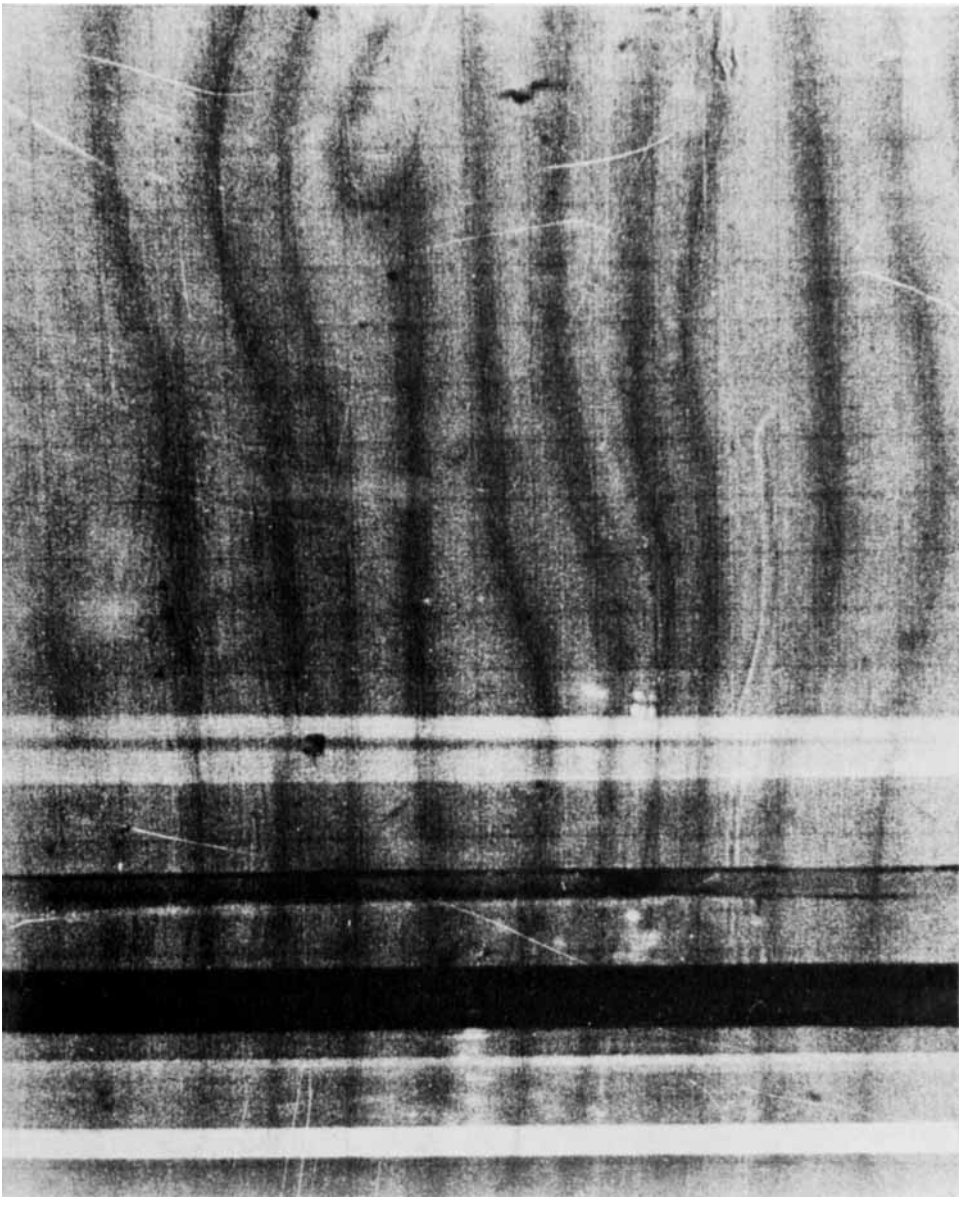

FIGURE 13. Convective overturning in the laboratory experiment. An S-shape in the lower part of the figure begins to fold, thus producing turbulence.

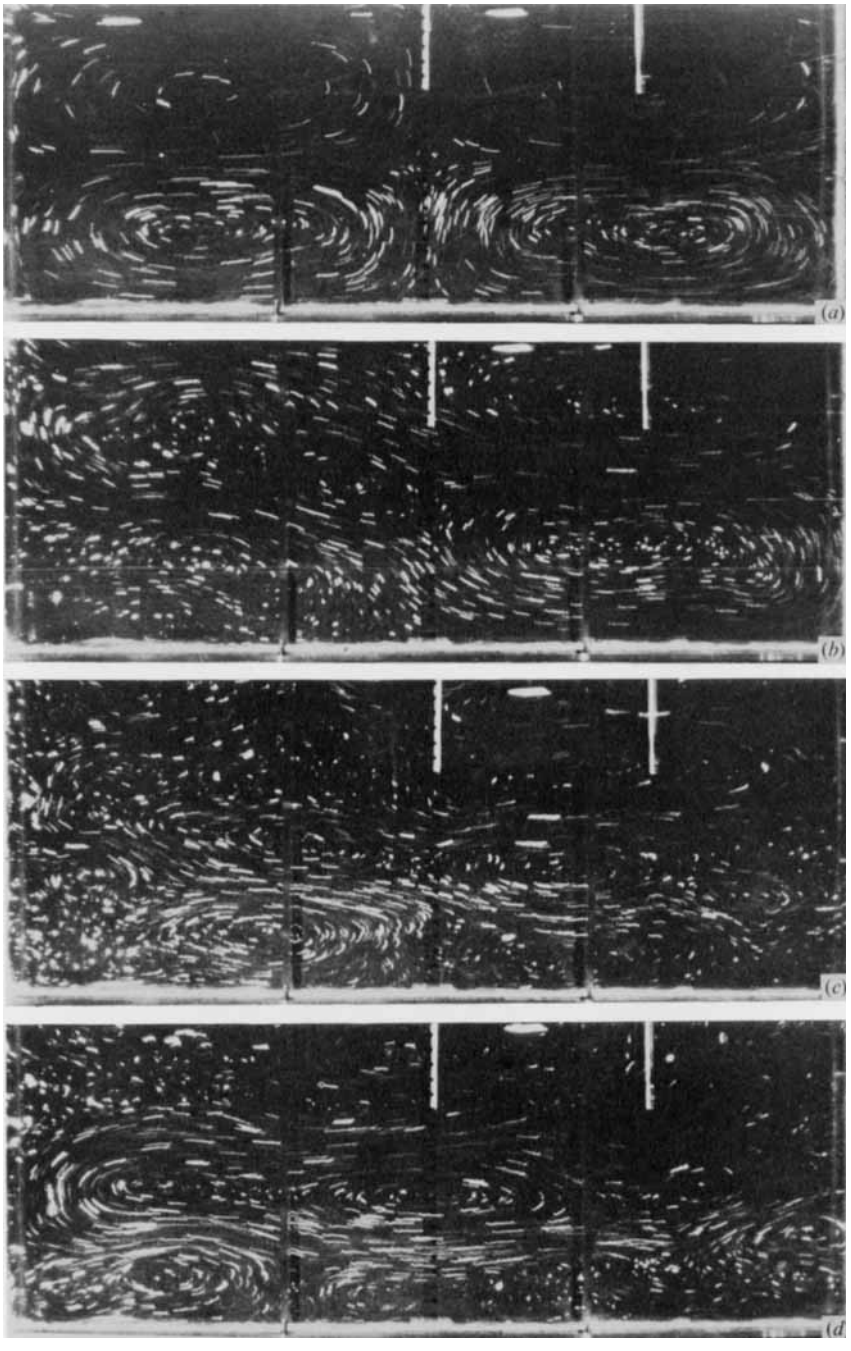

FIGURE 14. A sequence of pictures showing the trajectories at four stages of the breaking of standing waves for $n = 3$ (see text). (*a*) $t = 366{\cdot}5$ s. (*b*) $t = 929{\cdot}5$ s. (*c*) $t = 1896{\cdot}5$ s. (*d*) $t = 2221$ s.

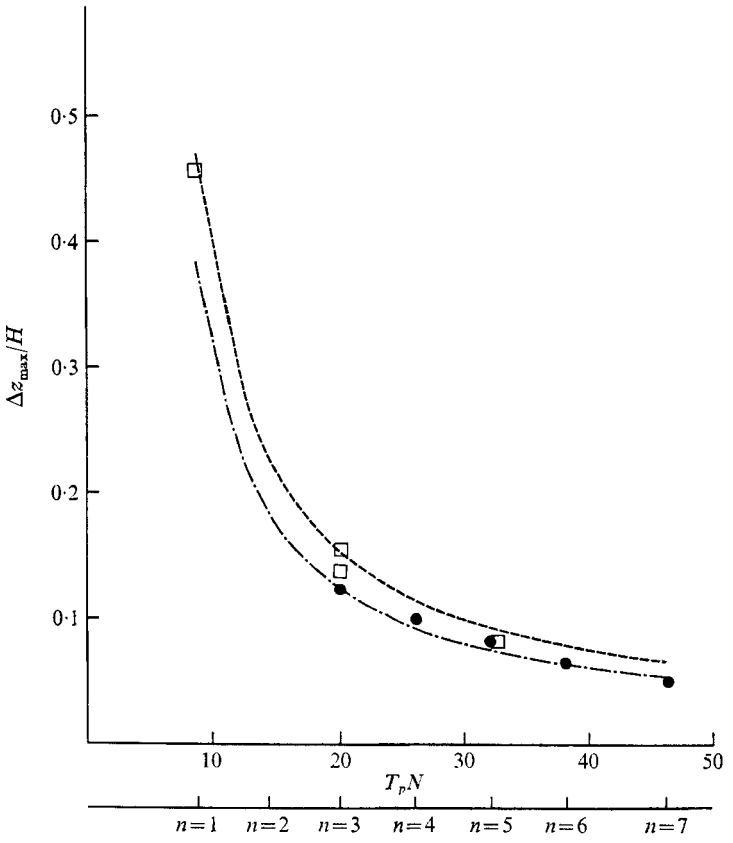

FIGURE 11. The critical amplitude as a function of the vertical wavenumber. – – –, equation (6.8); — · —, $(\Delta z/H)_{max} = 0{\cdot}64/n\pi$; ●, measured maximum displacements of the isopycnics; □, critical amplitude from numerical experiment.

The comparison between the critical amplitude as a function of the vertical wavenumber n and the experimental results is shown in figure 11; the dashed curve is the expression (6.8) and the solid circles are the measured maximum displacements of the isopycnics. From the experiment, in all cases (n = 3 to 7) the maximum amplitude of the wave occurs just before breaking. The open squares are the critical amplitude for the numerical experiment. In the latter, the wave amplitude increases a little more ($\sim 5\,\%$), but the solution at that point becomes unrealistic owing to the limited resolution. The data can be fitted by the (dashed–dot) curve $(\Delta z/H)_{exp} \approx 0{\cdot}64/\pi n$; the nonlinear terms neglected in the density expression (6.6) may account for the small differences between the two curves $(\Delta z)_{max}$ and $(\Delta z)_{exp}$.

The structure of the density field at the critical amplitude in the numerical solution, when n = 3, is shown in figure 12. Notice that in figure 12(*a*) the solution after a time of approximately 16 periods of oscillation shows a weak unstable density gradient just below the region of strong horizontal advection (for comparison see figure 8(*b*)). In figure 12(*b*) we can see that the solution just one period later shows stronger regions of unstable stratification. Unfortunately, the

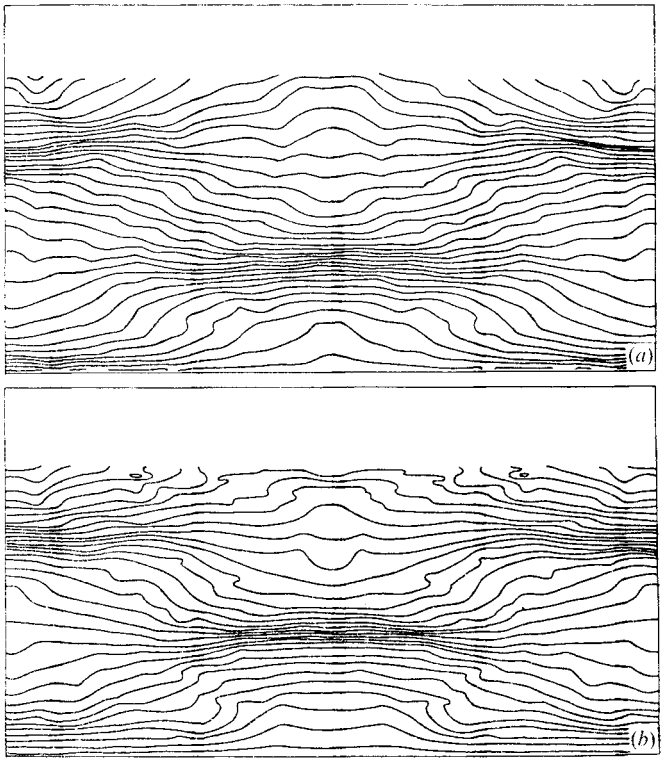

FIGURE 12. The density field structure at the critical amplitude from the numerical solution when $n = 3$. (*a*) At the moment when unstable density gradients are observed; $t = 16$ periods. (*b*) The result after one more period is shown; $t = 17$ periods.

numerical model has a limited resolution which does not enable one to give an accurate description of the overturning process.

One detail of convective overturning in the laboratory experiment, for the same n, is shown in figure 13 (plate 4). (This picture was retouched in order to increase the contrast of the layers.) In this picture we observe that when the density perturbation is a maximum a small region where the density gradient is unstable can be seen and then the density perturbation increases. At this point, the layer with the S-shape (see figure 12(*b*)) will start to fold, thus producing turbulence in that area of the wave with practically neutral density stratification. We can detect different behaviour patterns of the turbulence which are a function of the magnitude of the breaking. For example, if the regions are small, they tend to collapse into very thin layers which are eventually eliminated by diffusion. It is conceivable that this process is an explanation of the distortion in the standing waves which was found by McEwan (1971). On the other hand, larger regions will also collapse but they do interact with the mean wave. As a result of this interaction, a complete change in the large-wave characteristics sufficient to offset the resonant balance that the wave has at this point is produced, thus explaining the fact that when the waves start to break no increase in amplitude is observed. The effects are shown in figure 14 (plate 5).

In figure 14, four frames were put together, each showing the lower two-thirds of the tank. For this case $n = 3$, the period is 31·5 s, $N = 0{\cdot}6031\ \mathrm{s}^{-1}$ and the time exposure is 3 s. Now, in the first frame (figure 14(*a*)), where $t = 366{\cdot}5$ s or approximately 12 periods, the cells are regular and symmetric. The tracers, in the centre of the tank, show strips of about 2·6 cm, and since the time exposure is 3 s a vertical velocity of 0·9 cm/s can be estimated as well as the displacement $\Delta z/H = 0{\cdot}120$, which corresponds to a value very close to the maximum amplitude as shown in figure 11. The patches of turbulence slowly interact with the dynamics of the standing wave and, as we can see in figures 14(*b*) and (*c*), strong asymmetries develop. These sporadic patches try to interact with the cell's circulation as can be seen in figure 14(*b*). In doing so, the small eddies move around over a horizontal surface along the tank and at the end a secondary circulation builds up which covers the entire length of the tank. This is the case in figure 14(*d*), in which the structure can be described as layers of small eddies separated by strong jets. No vertical profiles of density were made at this point; however, some profiles were taken a half hour after stopping the paddle. At that time, the circulation was quite weak, but the profiles suggest the possibility that the layers formed by the small eddies had neutral stratification owing to strong mixing, whereas the layer with strong jets also had strong stratification. This type of circulation, as shown, is independent of both paddle frequency and wavenumber since similar circulations were found for other cases. We cannot be completely sure, however, that the tank walls are unimportant for this secondary circulation. The lack of resolution in the numerical model made a complete simulation of the secondary circulation impossible. However, some tendency for the asymmetry of the cell circulation was obtained when the numerical solution was perturbed close to the breaking amplitude with very small random disturbances at one instant.

A noteworthy point is that, if we look at the kinetic energy spectrum as a function of horizontal wavenumber, figure 14(*a*) will show a sharp peak at $k_0 = 2\pi/L$, the resonant wavenumber. In figure 14(*b*), more energy will flow to the higher wavenumbers from the resonant wave k_0. We may be inclined, intuitively, to relate this to any process that generates turbulence; however, in the end, these small eddies will tend to feed energy to the lower wavenumbers to build up the circulation shown in figure 14(*d*). This process closely resembles the reversed cascade effect produced in two-dimensional turbulence. Perhaps, in this case, the stratification maintains the two-dimensionality of the flow.

7. Dissipation of standing waves

The damping effect for the free waves, after the forcing has stopped, can be measured as a function of time. In most cases the amplitude Δz of the salinity probe signal decreases exponentially with time. An example of this is shown in figure 15, in which the amplitude Δz is plotted against the number of periods of the free waves on a semi-logarithmic scale. The rate of damping is given by the slope of the curve, and it should be pointed out that only the waves excited close to resonance give a response similar to this one. However, waves with frequencies

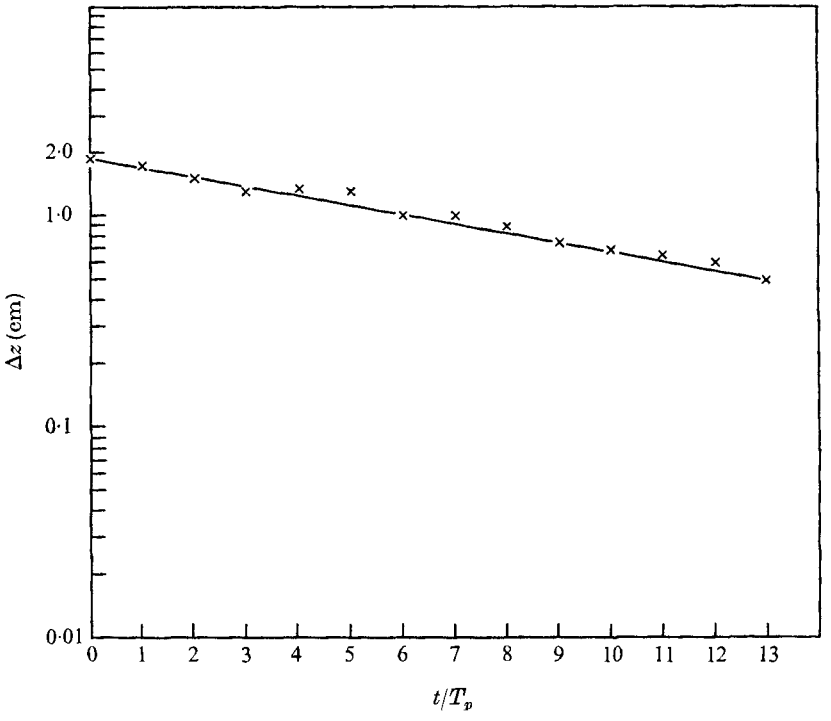

FIGURE 15. The amplitude of the free mode *vs.* time plotted on a semi-log scale.

between the resonant frequencies had an oscillatory response for the free modes which was probably because more than one mode was excited. In this latter case, we found that a decay time was difficult to estimate; therefore, these cases were not considered.

In order to estimate the damping, we can discriminate between the interior and boundary dissipation.

$$dE/dt = D_B + D_I, \tag{7.1}$$

the interior (D_I) and the boundary (D_B) dissipation being computed in a similar manner to that of Thorpe (1968). Following his analysis the amplitude of the free waves is given approximately by

$$\Delta z = \Delta z_0 e^{-qt} \tag{7.2}$$

and the damping rate is:

$$\frac{T_p}{\Delta z}\frac{d}{dt}\Delta z = qT_p, \tag{7.3}$$

where $q = q_I + q_B$. For a closed container q_I and q_B are given by

$$\left.\begin{aligned} T_p q_I &= \frac{\pi^3 \nu_M}{\omega H^2}(1+n^2), \\ T_p q_B &= \left(\frac{2\nu_M}{\omega H^2}\right)^{\frac{1}{2}} \pi \left[\frac{H}{D} + \frac{2n^2+1}{n^2+1}\right]. \end{aligned}\right\} \tag{7.4}$$

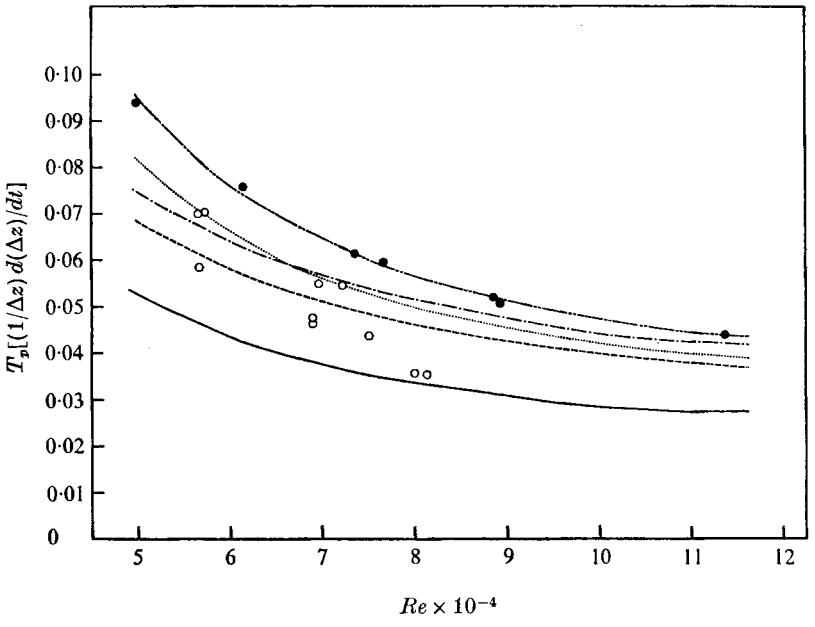

FIGURE 16. Non-dimensional damping as a function of the Reynolds number $Re = \omega H^2/\gamma_M$ ——, theoretical curve derived from (7.6) $\delta_B = 1$, $\delta_I = 1$. Experimental curves: – – –, $\delta_B = 0{\cdot}5$, $\delta_I = 1$; ·····, $\delta_B = 0{\cdot}5$, $\delta_I = 0{\cdot}5$; —·—, $\delta_B = 0{\cdot}4$, $\delta_I = 1$; —··—, $\delta_B = 0{\cdot}4$, $\delta_I = 0{\cdot}4$.

Substituting (7.4) into (7.3)

$$\frac{T_p}{\Delta z}\frac{d(\Delta z)}{dt} = \frac{\pi^3}{Re}(1+n^2) + \pi\left(\frac{2}{Re}\right)^{\frac{1}{2}}\left[\frac{H}{D} + \frac{2n^2+1}{n^2+1}\right], \tag{7.5}$$

where Re is the Reynolds number $\omega^2 H/\nu_M$ and n is the vertical wavenumber. The damping rate is not only a function of the Reynolds number through the frequency but also of the wavenumber n. Notice, however, that this dependence is only relevant in the interior dissipation term $1+n^2$. The dissipation term due to the boundaries $(H/D+(2n^2+1)/(n^2+1))$ for values of $n = 2, 3, 4$ is practically a constant $(H/D+2)$. In this case $H/D = 2{\cdot}5$ and therefore the constant equals 4·5.

Now, considering the possibility that we may have turbulence in the boundary layers as well as in the interior, we can modify (7.5) to contain an eddy viscosity for the boundary layer and one also for the interior; however, the two are not necessarily equal. So we can define two parameters $\delta_B = \nu_M/\nu_B$ and $\delta_I = \nu_M/\nu_I$, which involve a ratio of the molecular and some eddy viscosity. Now (7.5) can be written as

$$\frac{T_p}{\Delta z}\frac{d(\Delta z)}{dt} = \frac{\pi^3\delta_I}{Re}(1+n^2) + 4{\cdot}5\left(\frac{2\delta_B}{Re}\right)^{\frac{1}{2}}. \tag{7.6}$$

The non-dimensional damping observed is plotted in figure 16 *vs.* the Reynolds number and the theoretical curve (7.6) for different values of δ_I and δ_B also appears there. The results show damping larger than the molecular viscosity predicts ($\delta_I = \delta_B = 1$). An estimate of an eddy viscosity equal to about 2 or 3 times the molecular viscosity seems reasonable and fits the waves in which breaking is visible (solid circles).

8. Conclusion

A solution to the transient behaviour of the resonant growing standing waves was found by using a perturbation expansion. The solution was compared with laboratory experiments as well as a numerical nonlinear solution of the same problem. The conclusions are as follows.

(i) The transient behaviour and the nonlinear tendency of the standing waves are described well by the analytic expression.

(ii) The numerical results describe the solution very well until the wave starts to break.

(iii) From the laboratory experiment and the numerical results it can be concluded that the standing internal gravity waves break because of local gravitational instability at a critical amplitude close to the one predicted by the expansion theory.

(iv) This amplitude seems to be the maximum amplitude that a wave can reach.

(v) When the generation of turbulence is violent, the small eddies start to force a secondary flow characterized by layers of strong jets separated by patches of turbulence.

I would like to express my thanks to Prof. G. Mellor, Prof. G. Mattingly and Prof. G. Stegen for their assistance in designing the laboratory experiment, to several colleagues at the Geophysical Fluid Dynamics Laboratory for their help, particularly Dr K. Bryan and Dr K. Miyakoda, and to Dr B. B. Ross and Mr L. Polinsky for their assistance with the numerical program, the analysis of data and general suggestions which helped to clarify the paper. My thanks also to Mr E. Wolensky and the personnel of the Aerospace and Mechanical Science Department of Princeton University for their help in taking the measurements and building the required instruments and to Mrs Y. Towns for typing the manuscript. This work was partially supported by N.S.F. grant GA-14955 to Princeton University.

REFERENCES

FORTUIN, J. M. H. 1960 Theory and application of two supplementary methods of construction of density gradient columns. *J. Polymer Sci.* **44**, 505–515.

LIPPS, F. B. 1971 Two-dimensional numerical experiments in thermal convection with vertical shear. *J. Atmos. Sci.* **28**, 3–19.

MCEWAN, A. D. 1971 Degeneration of resonantly-excited standing internal gravity waves. *J. Fluid Mech.* **50**, 431–448.

ORLANSKI, I. 1971 Energy spectrum of small-scale internal gravity waves. *J. Geophys. Res.* **76**, 5829–5835.

ORLANSKI, I. & BRYAN, K. 1969 Formation of the thermocline step structure by large amplitude internal gravity waves. *J. Geophys. Res.* **74**, 6975–6983.

PHILLIPS, O. M. 1966 *The Dynamics of the Upper Ocean.* Cambridge University Press.

THORPE, S. A. 1968 On standing internal gravity waves of finite amplitude. *J. Fluid Mech.* **32**, 489–528.